ELSEVIER

Chemical Engineering Science 63 (2008) 2075–2085

Chemical Engineering Science

www.elsevier.com/locate/ces

X-ray computed tomography of a gas-sparged stirred-tank reactor

Jason J. Ford[a], Theodore J. Heindel[a,*], Terrence C. Jensen[b], Joshua B. Drake[a]

[a]*Department of Mechanical Engineering, Iowa State University, Ames, IA 50011-2161, USA*
[b]*Center for Nondestructive Evaluation, Iowa State University, Ames, IA 50011-2161, USA*

Received 19 September 2007; received in revised form 21 December 2007; accepted 2 January 2008
Available online 15 January 2008

Abstract

X-ray computed tomography (CT) is used to explore the differences in gas dispersion in a stirred-tank reactor (STR) for different operating conditions by varying the impeller speed and gas flow rate. X-ray imaging has been carried out in a 0.21 m ID acrylic STR equipped with a nylon Rushton-type impeller. From the CT images, major differences in local gas holdup are observed for different operating conditions. Completely dispersed conditions have a relatively uniform holdup profile while flooded conditions show a high gas holdup near the impeller shaft. The high resolution of the X-ray system allowed fine details such as recirculation regions behind the baffles to be visualized.

Keywords: Hydrodynamics; Multiphase flow; Stirred-tank reactor; Tomography; Visualization; Voidage

1. Introduction

Stirred-tank reactors (STRs) are often used in the process industries to carry out reactions between liquids and gases. Gas holdup, which is defined as the volumetric gas fraction, is one of the most important hydrodynamic parameters needed for reliable design, performance estimation, and scale-up of these reactors. Gas holdup depends on the gas and liquid properties, superficial gas velocity, presence of solids, sparger and impeller design, reactor internals, and power consumption. In order to better design STRs, it is highly desirable for engineers to know the local gas holdup (ε_g) and how it changes with different operating conditions. The knowledge of local gas holdup can also be used for validating computational fluid dynamic (CFD) codes and for advancing the understanding of mixing fundamentals.

The flow patterns of an STR are complicated and have been studied by many authors (Ranade and Deshpande, 1999; Smith and Warmoeskerken, 1985; Van't Riet, 1975; Van't Riet and Smith, 1975). A gas-sparged STR generally goes through four well-defined flow regimes of flooded, loaded, completely dispersed, and gas recirculation, depending on gas flow rate, Q_g, and impeller speed, N (Nienow et al., 1985). The flooded condition ($0 < N < N_f$) is undesirable and characterized by an axial rise of gas to the surface with little dispersion. When $N = N_f$, the flow transitions from flooded to loaded. In the loaded regime ($N_f < N < N_{cd}$), the impeller is better able to radially distribute the gas, but there is still poor gas distribution throughout the vessel due to the buoyant forces of the gas being larger than the radial drag force resulting from liquid mixing. The flow transitions to completely dispersed flow when $N = N_{cd}$. The completely dispersed regime ($N_{cd} < N < N_r$) is a highly desirable operating regime due to the gas being completely dispersed at a low power input. Finally, gas recirculation is observed when $N = N_r$. Much work has been done to identify the transition between these regimes (Kapic and Heindel, 2006; Nienow et al., 1985, 1977; Warmoeskerken et al., 1981; Warmoeskerken and Smith, 1982).

Global gas holdup ($\varepsilon_{g,t}$) can easily be measured visually by looking at the difference in liquid height when gas is sparged (H_D) compared to the liquid height (H) with no gas being sparged (Rushton and Bimbinet, 1968; Saravanan and Joshi, 1996; Yawalkar et al., 2002):

$$\varepsilon_{g,t} = \frac{H_D - H}{H_D}. \tag{1}$$

When the tank is mechanically agitated or the gas flow rate is high, liquid surface fluctuations lead to subjectivity in

* Corresponding author. Tel.: +1 515 294 0057; fax: +1 515 294 3261.
E-mail address: theindel@iastate.edu (T.J. Heindel).

0009-2509/$ - see front matter © 2008 Elsevier Ltd. All rights reserved.
doi:10.1016/j.ces.2008.01.007

determining the liquid height. In an attempt to reduce the subjectivity in the measurement, H_D may be measured at two locations diametrically opposite to each other and between two adjacent baffles (Saravanan and Joshi, 1996). Saravanan and Joshi (1996) determined global gas holdup visually and report that when $\varepsilon_{g,t}$ was less than 0.03, the reproducibility was within 15%. At higher values of holdup, the reproducibility improved to within 10%.

Measuring local gas holdup is extremely difficult because invasive probes are just that, invasive, and they only provide a point source measurement; still many authors have utilized invasive methods to measure local gas holdup in STRs (Bombac et al., 1997; Boyer et al., 2002; Favre et al., 1993; Greaves and Barigou, 1988; Lu and Ju, 1987; Nagase and Yasui, 1983; Nienow et al., 1977; Takenaka and Takahashi, 1996; Wang et al., 2006). Tomographic measurement methods provide an alternative approach to measuring local gas holdup. They have the advantage of being nonintrusive, and they can provide a large measurement region during a single data acquisition event.

Noninvasive measurement techniques have been reviewed in the literature; the non-radiation based tomographic techniques include ultrasound (Chaouki et al., 1997; Fischer et al., 1992; Kumar et al., 1997; Supardan et al., 2004; Utomo et al., 2001), electrical capacitance tomography (ECT) (Chaouki et al., 1997; Halow, 1996; Warsito and Fan, 2001), and electrical resistance tomography (ERT) (Chaouki et al., 1997; Holden et al., 1998; Wang et al., 2000). Many of these techniques have limitations or drawbacks when implemented. For example, ultrasound has good spatial resolution of approximately 3% of the object diameter (Warsito et al., 1999), but long temporal resolution and a complicated data analysis procedure (Supardan et al., 2004; Utomo et al., 2001). Fischer et al. (1992) used ultrasound in an STR and estimated the accuracy of gas holdup to be around 15%. In ECT and ERT systems, the electric field utilized is called soft because measurements are not only a function of the voidage, but also a function of the electrical properties and temperature of the medium (Kumar et al., 1997). ECT and ERT have great temporal resolution but the spatial resolution is on the order of 5% of the object diameter (Holden et al., 1998; Warsito and Fan, 2005).

X-ray and γ-ray computed tomography (CT) are two radiation based techniques. The basis of radiation imaging techniques is that gases, liquids, and solids have different radiation absorption coefficients. When X-rays or γ-rays are transmitted through a heterogeneous medium, attenuation measurements provide a measure of the local mass density along the path traversed by the beam (Chaouki et al., 1997). By taking measurements of different beam paths at different spatial and angular orientations, a density distribution of phases with high spatial resolution can be obtained after a reconstruction procedure. Because the data collection is automated and performed by a computer, the process is referred to as computed tomography (CT). The local gas holdup for both techniques is time-averaged due to the length of the data collection process.

Thatte et al. (2004) used a 67 μCi ^{137}Cs source (γ-ray) to measure gas holdup in a transparent, flat-bottom, 0.57 m diameter cylindrical tank equipped with a pitched-blade downflow turbine or a disk turbine. For both impellers, the average gas holdup was obtained by integrating the local gas holdup and it matched well with the results obtained by visual observations. The reproducibility of the measurements was within $\pm$10%. Khopkar et al. (2005) used a ^{137}Cs source with seven NaI detectors to measure gas holdup in a flat-bottomed 0.2 m diameter cylindrical tank with a shaft that extended to the vessel bottom. The total scan time was a little over 3 h. Khopkar et al. (2005) noted that CT results were sensitive with respect to the convergence criterion used during data processing. High energy γ-rays, unlike X-rays, also work on larger tanks because the γ-rays are strong enough to pass through substantial thicknesses of metals, overcoming the reactor wall thickness. For example, Veera et al. (2001) used a ^{137}Cs source to measure gas holdup in a three-phase 4.9 m diameter stirred-tank reactor equipped with 2 impellers.

This current study uses X-ray attenuation to measure local time-averaged gas holdup in a stirred-tank reactor. Compared to γ-ray tomography, X-ray tomography allows for better spatial resolution due to the better match between available X-ray sources and high-resolution X-ray imagers. However, X-rays lack the penetrative power of γ-rays and are better suited for smaller test sections. Hence, the focus of this study is on a 21 cm ID STR.

2. Experimental methods

2.1. Stirred-tank reactor

Experiments are carried out in a custom-built acrylic STR that is comparable in size and shape to a BioFlo 110 Fermenter (New Brunswick Scientific Co.), which is an off-the-shelf STR used for fermentation and academic studies. The dished-bottomed tank (Fig. 1a) is made from acrylic to minimize image artifacts during the CT scans (Ketcham and Carlson, 2001). The reactor has an internal diameter of $T = 21$ cm. The tank walls are 0.64 cm thick. As shown in the plan view in Fig. 1b, the tank has four equally spaced baffles of width 1.8 cm and thickness 0.6 cm glued directly to the tank wall and run the entire tank height. Tap water is used as the working fluid and filled to a height of $H = T$, which corresponds to a working volume of approximately 7 l.

The impeller shaft and Rushton-type impeller are both made out of nylon because acrylic is too brittle. The six-blade Rushton-type impeller has a diameter D=7.6 cm (D=0.36T). The impeller blades have a height of 1.9 cm and a thickness of 0.3 cm. The impeller hub has a diameter of 3.1 cm. Unlike most STRs, the nylon shaft used in this study penetrates the bottom of the tank to provide stability and reduce vibration. The hole in the acrylic STR bottom into which the shaft is inserted also acts as a bearing (Fig. 1c); if the shaft did not rest in this hole during operation, the flexible nylon shaft would wobble violently. The impeller is located 5.7 cm from the STR bottom, which corresponds to a clearance $C = 0.27T$. Gas is introduced into the tank through a 5.1 cm diameter acrylic ring sparger with nine 1 mm diameter holes (Fig. 1c). The ring

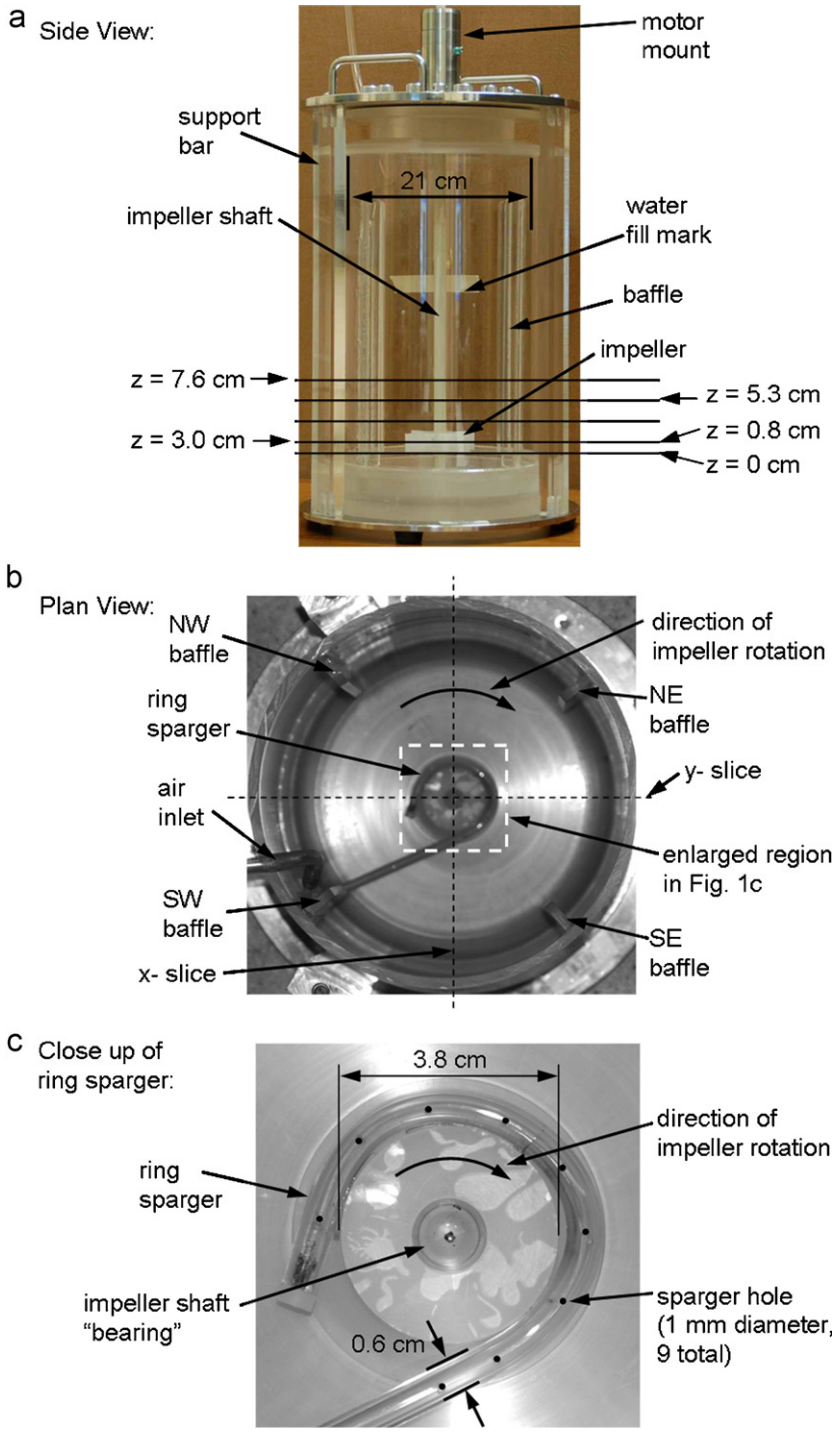

Fig. 1. STR used in this study: (a) side view, (b) plan view, and (c) close up of ring sparger.

sparger is attached to the STR bottom and wrapped around the shaft bearing instead of being located off the bottom (typical of most STRs). The impeller is driven by a variable speed DC motor mounted on the top of the STR and connected to a BioFlo 110 Primary Control Unit (PCU) manufactured by New Brunswick Scientific Co. The motor and STR top are from the BioFlo 110 STR. Additional details of the STR used in this study are provided by Ford (2006).

2.2. Power measurements

The motor used to drive the impeller is manufactured by Magmotor Corporation (model number C32-E-450X). For measuring power consumption, an Electro model PS-5R rectifier is used to supply the motor with a constant DC voltage. The power draw is measured by connecting an EXTECH Instruments True RMS Power Analyzer in parallel between the PCU

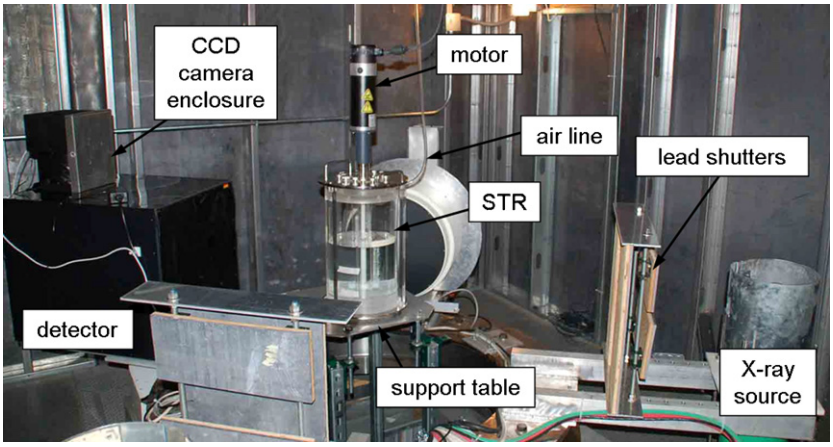

Fig. 2. X-ray system setup.

and the DC power supply. The actual mixing power imparted to the fluid, P_g, is then determined from the difference between the measured power with and without fluid in the vessel, while operating at a given impeller speed; this accounts for frictional losses in the motor. The desired impeller speed (N) is obtained by adjusting the power supply and is measured by an internal tachometer in the PCU.

The standard error values for the power measurements ranged from 0.04 to 0.48 W. Percent standard error values ranged from 0.42% to 23.5%, with most values below 10%. The measurements made at the lower impeller speeds tended to have a higher percent standard error.

2.3. X-ray imaging

The X-ray system used in this study (Fig. 2) has been described elsewhere (Heindel et al., 2005, 2007, 2008; Hubers et al., 2005) and only a summary is provided here. The X-ray source is a LORAD LPX200, which has a focal spot of 1.5 mm. The source emits a conical X-ray beam and allows for multiple CT slices to be acquired during a single scan. A 1 mm copper filter is placed in front of the tube to suppress low energy radiation. The unit is liquid cooled and has an adjustable voltage (10–200 kV) and current (0.1–10.0 mA), with a maximum power output of 900 W.

A 44 × 44 cm cesium-iodide scintillator screen is used to convert the X-rays into light that is viewed through a 50 mm Nikon lens connected to a CCD camera. The detector is on a movable slide which enables the magnification factor to be adjusted. The CCD camera used to digitize the image is an Apogee Alta U9 system with a sensor array of 3072(H) × 2048(V) pixel, with a pixel size of 9 μm × 9 μm. The CCD camera is thermoelectrically cooled, allowing longer exposures with low-noise, thereby making it well suited for providing superior CT images. The camera has various binning capabilities (resolution settings). A 4 × 4 binning was used in this study; hence, each reconstructed pixel physically represents 0.6 mm. Note that one of the advantages of using an X-ray CT system is the excellent spatial resolution which, in this study, is 0.3% of the STR diameter. An exposure time of 1 s. was used in this study to provide a compromise between image acquisition time and signal strength.

The source and camera are mounted on a slewing ring with an ID of 1.0 m, which allows the source and detector to rotate around the STR during a CT scan. The ring is rotated by a Parker stepper motor with a limit switch attached at the position assigned 0° to prevent the cooling, power, and data cables from being wrapped around the STR stand.

X-ray CT imaging produces images of a cross-sectional plane (slice) through an object. A CT slice is a quantitative map of the linear X-ray attenuation coefficient μ. Since the X-ray system used in this study emits a conical beam, multiple slices can be acquired during a single scan, thereby producing a volumetric rendering of the object. The slice is created by acquiring images at different angular orientations. For the data taken in this study, X-ray images were taken at 136 kV and 5.7 mA at every 1° around a 360° path. Since it takes time to acquire the 360 images, the data in a reconstructed CT image are a time-average of the events during the acquisition period. In this study, a typical scan lasts approximately 45 min with the camera binning option set to 4 × 4 and a single frame exposure time of 1 s.

Image acquisition for the system is controlled by a personal computer with 4 GB of RAM and custom software developed by the Center for Nondestructive Evaluation (CNDE) at Iowa State University (Zhang et al., 2005). Algorithms were created to take care of individual pixel nonuniformity and beam hardening, which are common in X-ray CT and described by Ford (2006). Image reconstruction utilizing filtered back projection is completed in less than 5 min on a 64-node LINUX cluster at the CNDE.

3. Results

3.1. Power measurement

For this study, power measurements were taken with constant gas flow rates of $Q_g = 6$, 9, and 12 LPM while varying the impeller speed in increments of 25 rpm. Fig. 3 shows the gassed power number (N_{pg}) as a function of the gas flow

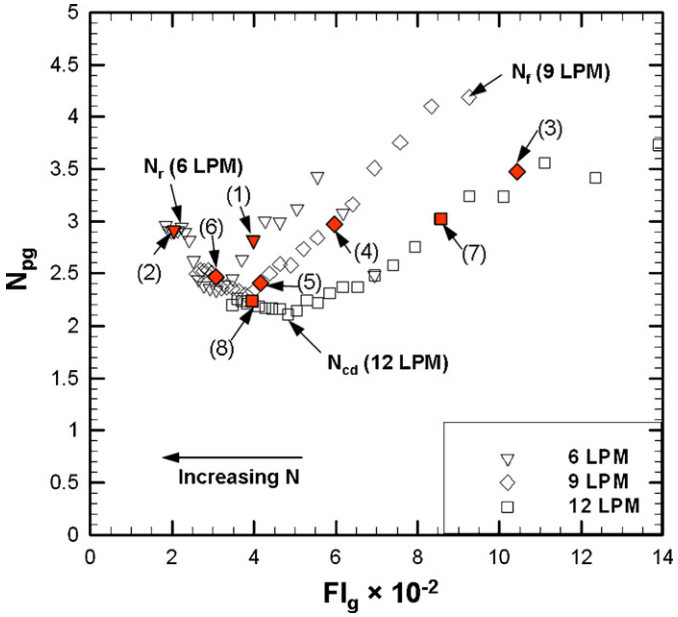

Fig. 3. Gassed power number vs. flow number at constant gas flow rate. Numbers in parentheses correspond to locations of CT images as described in the text.

number (Fl_g), where

$$N_{pg} = \frac{P_g}{\rho_L N^3 D^5}, \tag{2}$$

$$\mathrm{Fl}_g = \frac{Q_g}{ND^3}. \tag{3}$$

In these expressions, P_g is the measured mixing power and ρ_L is the fluid density.

For the custom STR used in this study, the ungassed power number varied from 4.3 to 5.2, with a slight dependence on N (Ford, 2006). For STRs operating in the turbulent regime, ungassed power numbers are nearly constant (Nienow, 1998). For STRs with Rushton-type impellers, the ungassed power number has been reported to be ~ 5 (Nienow, 1998). The average ungassed power number for the system used in this study is 4.8.

The regime transition speeds of N_f (flooding/loading), N_{cd} (loaded/completely dispersed), and N_r (completely dispersed/recirculation) were found by power measurements and were in good agreement with visual observations (Ford, 2006). Following Figliola and Beasley (2000), the uncertainty in N_{pg} and Fl_g are on the order of $\pm 15\%$ and $\pm 6\%$, respectively, with most conditions falling well under these values.

When looking at Fig. 3, it should be noted that the impeller speed increases from right to left. At low impeller speeds and high gas flow rates (high gas flow number, high gassed power number), flooding occurs, which is characterized by a bubble column flow where the bubbles rise vertically and are virtually unaffected by the rotating impeller. Flooding is the least desirable operating regime due to the lack of dispersion, which leads to a low gas holdup and low mass transfer rates. Further increases in impeller speed lead to the flooding/loading transition (N_f) characterized by a local maximum on the graph. To the right of N_f, the impeller is flooded, while to the left of N_f, the tank is said to be loaded and the impeller acts to disperse the bubbles radially outward in the upper part of the vessel.

As the impeller speed increases, the transition to complete dispersion occurs at the local minimum N_{cd} (Nienow et al., 1977). Complete dispersion corresponds to the point at which bubbles are dispersed throughout the tank, including the area below the impeller. For efficient operation, which corresponds to high gas holdup and high mass transfer rates, the impeller speed should be greater than or equal to N_{cd}; this is a desirable impeller operating speed because bubbles are dispersed throughout the tank at the lowest possible power input. Further increases in impeller speed reveal another local maximum (N_r). When the impeller has reached N_r, secondary circulation loops form and gross gas recirculation occurs (Nienow et al., 1977).

The locations of the CT scans described in this paper are identified by the solid symbols in Fig. 3 and correspond to: (1) $Q_g = 6$ LPM and $N = 350$ rpm; (2) $Q_g = 6$ LPM and $N = 700$ rpm; (3) $Q_g = 9$ LPM and $N = 200$ rpm; (4) $Q_g = 9$ LPM and $N = 350$ rpm; (5) $Q_g = 9$ LPM and $N = 525$ rpm; (6) $Q_g = 9$ LPM and $N = 700$ rpm; (7) $Q_g = 12$ LPM and $N = 325$ rpm; and (8) $Q_g = 12$ LPM and $N = 700$ rpm.

3.2. CT visualization

To minimize detector nonuniformities (Ford, 2006), an image region corresponding to one impeller diameter in height was chosen. The region (Fig. 1a) starts at the bottom of the impeller ($z = 0$ cm) and traverses vertically upward one impeller diameter ($z = 7.6$ cm). This imaging region was selected due to the differences in flow regimes around the impeller for different operating conditions. There are a total of 200 slices in the imaging region, each having a thickness of 0.38 mm in the STR axial direction.

The local time-averaged gas holdup can be obtained from the CT values (Hammer et al., 2006) by using

$$\varepsilon_g = \frac{\mu/\mu_w - 1}{\mu_g/\mu_w - 1}, \tag{4}$$

where μ represents the linear attenuation coefficient, and the subscripts w and g represent the STR filled with water-only and gas-only, respectively. The value for μ_g is determined by taking a CT scan of an empty STR. To get an accurate value for μ_g, the values along five vertical lines comprising a total of 1000 values (i.e., 5 points in each of the 200 slices) are averaged. The value of μ_w is determined by taking a CT scan of the STR filled with water and no impeller rotation. Because the impellers were not moving in the water-only CT scan, whereas they were in the rest of the scans, there will be some image artifacts present in the CT images in the impeller region. Any bias is minimized by using nylon impellers, which attenuate X-rays similar to that of water.

To reduce noise in the data, a $3 \times 3 \times 3$ averaging technique was applied to all values. This average includes nine values from the slice above, nine values from the slice of interest, and nine values from the slice below, constituting a cubic average

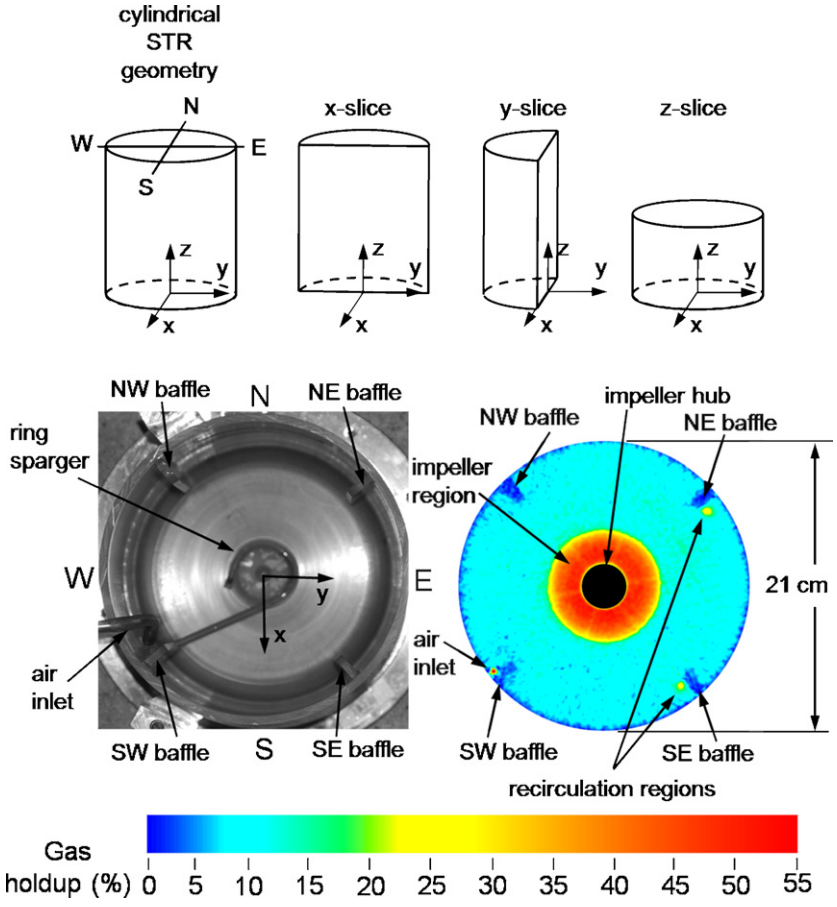

Fig. 4. CT image coordinate system and sample z-slice for $Q_g = 9$ LPM and $N = 700$ rpm.

for each time-averaged local gas holdup value. The averaged gas holdup values were then mapped to an 8-bit color scale for presentation. It should be noted that the mapping of gas holdup values is only applied for qualitative analysis. All quantitative analysis is done using the unmapped gas holdup values obtained from the CT data, which were acquired using 32-bit precision.

Custom software is available at the CNDE that allows for visualization of the CT data along all three axes (Zhang et al., 2005). The x- and y-slices presented below are side views through the tank center from two mutually perpendicular directions (Fig. 4), which show the difference in vertical gas dispersion for different operating conditions. The z-slices, which are plan views seen from looking straight down onto the tank, provide knowledge of how the local gas holdup varies radially and azimuthally. The 3D visualization software allows viewing of the data from any slice in the three directions.

Fig. 4 shows the orientation of the three slice planes and the directional orientation in the z-slice (i.e., N, S, E, and W). A sample z-slice image and the corresponding gas holdup color map are also shown. The orientation of this image corresponds to the accompanying STR plan view. Even though the impeller shaft and hub are solid regions, noise and reconstruction artifacts produce small positive and negative gas holdup values when using Eq. (4). Therefore, for all images presented in this study, the impeller shaft and hub regions are forced to $\varepsilon_g = 0\%$.

The impeller region in Fig. 4, represented by a high gas holdup (red) region, has a larger diameter than the actual impeller with the extent depending upon Q_g and N. The images shown here are cropped so that the edge corresponds to the inner edge of the tank wall with ID = 21 cm. The red spot in the bottom left of all the z-slice images (SW baffle) corresponds to the air inlet hose. The dark blue regions in the four "corners", which can be seen in the images taken while operating in the completely dispersed regime, are the four baffles. The yellow circular regions downstream of the NE and SE baffles are recirculation regions.

3.3. Qualitative observations

3.3.1. Flooded regime

As determined from the power consumption plot, $Q_g = 9$ LPM and $N = 200$ rpm (location (3) in Fig. 3) corresponds to the flooded regime. This is clearly seen in slice $z = 0.8$ cm (Fig. 5), where very little gas is located outside the impeller region. As the vertical distance increases from the impeller ($z = 3.0$, 5.3 cm), the central region of high gas holdup expands radially due to the decreased pressure head acting on the bubbles and the decreased bubble rise velocity which was also seen by Khopkar et al. (2005). As the bubbles spread out, there is an increase in drag which causes a lower bubble rise

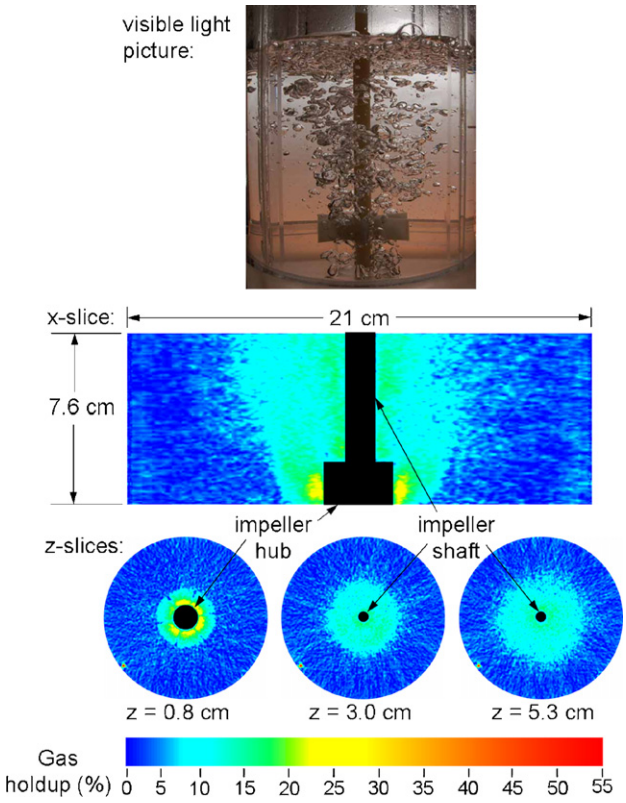

Fig. 5. Flooded flow regime at $Q_g = 9$ LPM and $N = 200$ rpm.

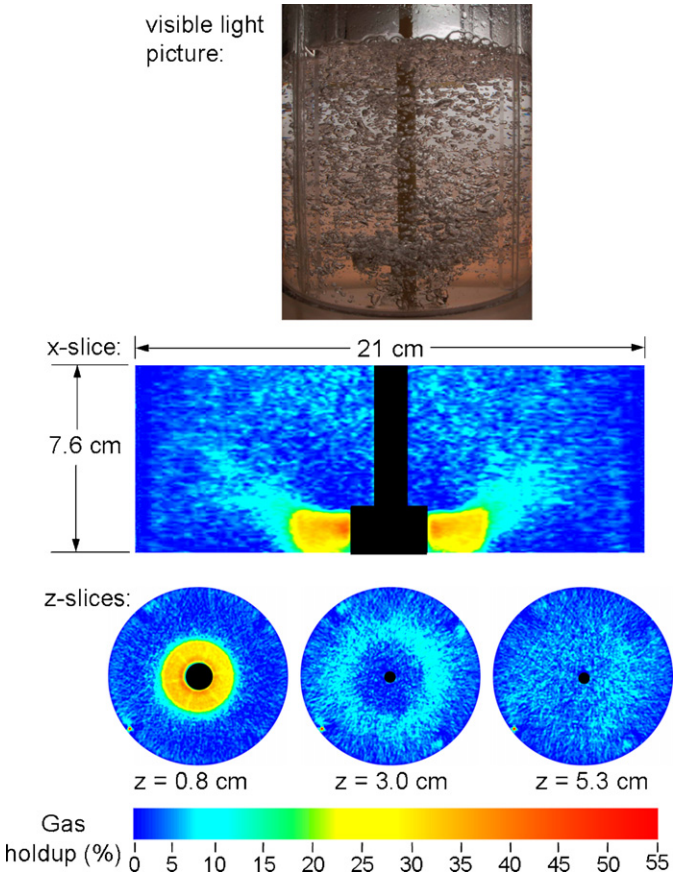

Fig. 6. Loaded flow regime at $Q_g = 9$ LPM and $N = 350$ rpm.

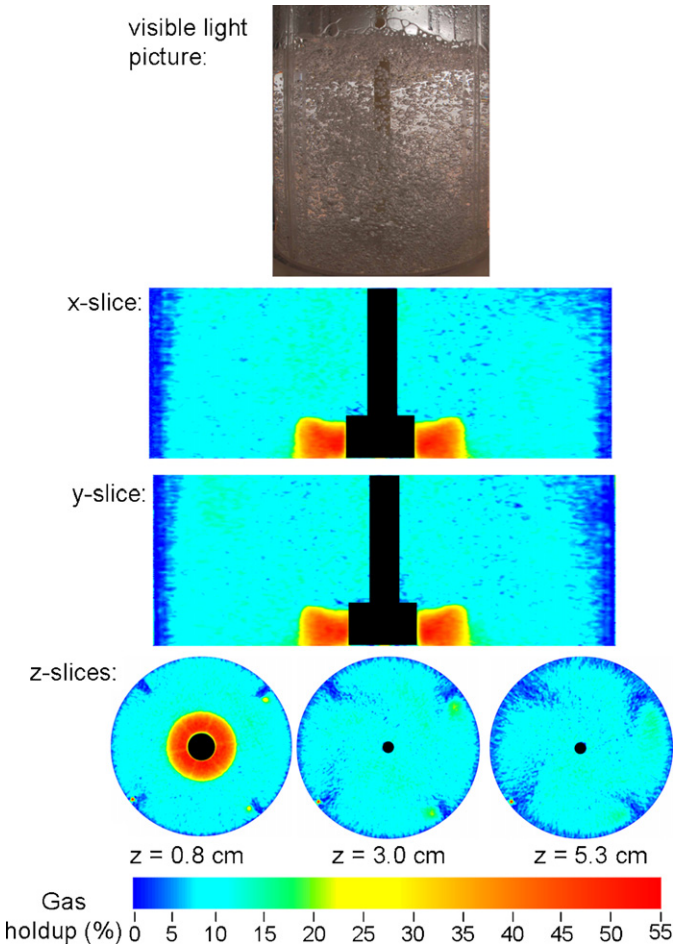

Fig. 7. Completely dispersed flow regime at $Q_g = 9$ LPM and $N = 700$.

velocity, thereby increasing the local gas holdup. The x-slice shows that the STR has an axial flow of gas through the impeller plane, which is defined by Warmoeskerken and Smith (1985) as flooded. It should be noted that the x-slice covers the imaging region in Fig. 1 thereby having a height of 7.6 cm and width 21 cm. The x-slice compares well with the accompanying visible light picture, which also shows the large bubble size for these conditions. There are very few bubbles near the tank walls, which is common of the flooded region. Note that in the visible light pictures presented here, the impeller is actually moving but a digital camera shutter speed of 1/4000 s allows for stop-motion images.

3.3.2. Loaded regime

When the impeller speed is increased to $N = 350$ rpm at a constant $Q_g = 9$ LPM (loaded regime; location (4) in Fig. 3), the gas is slightly dispersed. At $z = 0.8$ cm (Fig. 6), the gas is still located mainly around the impeller. The $z = 3.0$ cm slice has a distinct region of low gas holdup near the center and is the result of gas passing around the impeller hub and "thrown" radially outward. The x-slice shows regions of high gas holdup off the impeller tips due to the onset of the impeller dispersing the gas. Visually, the bubbles have decreased in size and are located throughout a larger region of the STR, as shown by

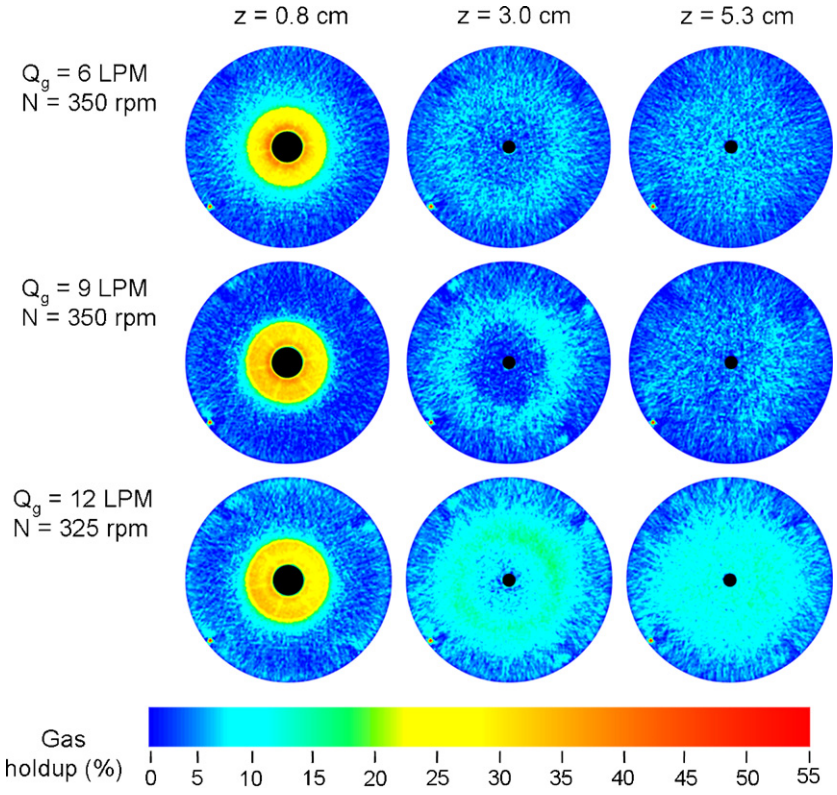

Fig. 8. CT images of the loaded flow regime at three different operating conditions corresponding to locations 1, 4, and 7 in Fig. 3.

the visible light picture. Below the impeller, there are very few bubbles, which is characteristic of the loaded regime.

3.3.3. Completely dispersed regime

At an impeller speed of $N = 700$ rpm and gas flow rate of $Q_g = 9$ LPM (location (6) in Fig. 3), power consumption measurements indicate the flow is completely dispersed, and the CT images show high gas holdups throughout the entire imaging region, which are higher than those for the other two conditions (Fig. 7). Recirculation cells are clearly visible in the lower two slices on the trailing edges of the NE and SE baffles. The recirculation zones only appear behind two baffles due to the slightly asymmetric gas entry caused by the sparger (Ford, 2006) (see also Fig. 1c). The x- and y-slice (view 90° from the x-slice) show a fairly uniform gas distribution. In the top-right corner of the x-slice, there is a region of lower gas holdup which is not seen in the top-left corner. Similar observations are found in the y-slice. The small asymmetries in the local gas holdup were common for all the images due to the unequal gas entrance caused by the manufacturing constraints on the sparger and are discussed in detail by Ford (2006). Bubbles have further decreased in size and are now located throughout the STR as shown by the visible light picture.

3.3.4. Flow regime comparison

Slices taken in the same flow regime have similar gas holdup distributions even though the gas flow rate and impeller speed are different. Fig. 8 shows the z-slices for: $Q_g = 6$ LPM with $N = 350$ (location (1) in Fig. 3), $Q_g = 9$ LPM with $N = 350$ (location (4) in Fig. 3), and $Q_g = 12$ LPM with $N = 325$ (location (7) in Fig. 3). As determined by power consumption measurements and visual confirmation, the above three conditions are all in the loaded regime. The $z = 0.8$ cm slice has gas located mainly around the impeller region. At $z = 3.0$ cm, there is a donut-shaped region of high gas holdup for all images due to the gas passing around the impeller hub. The top slices ($z = 5.3$ cm) look similar with $Q_g = 12$ LPM having a higher gas holdup due to more gas being sparged. The same results hold true for other conditions.

3.4. Quantitative measurements

3.4.1. Local holdup

Local time-averaged gas holdup values along the x-axis are plotted in Fig. 9 for $Q_g = 9$ LPM with impeller speeds $N = 200$ rpm (flooded), $N = 350$ rpm (loaded), and $N = 700$ rpm (completely dispersed) at $z = 0.8$ cm. For all plots, the negative distance corresponds to the southern portion of the tank (Fig. 4). The impeller hub region is blank since the gas holdup in this region is 0. For all three impeller speeds, the gas holdup rises dramatically in the impeller region due to the presence of cavities behind the stirrer blades (Van't Riet and Smith, 1975). A maximum time-averaged gas holdup in this region is less than 55% for these conditions. For $N = 700$ rpm (completely dispersed), the holdup is higher outside the impeller region than for the other two impeller speeds. At lower impeller speeds, the

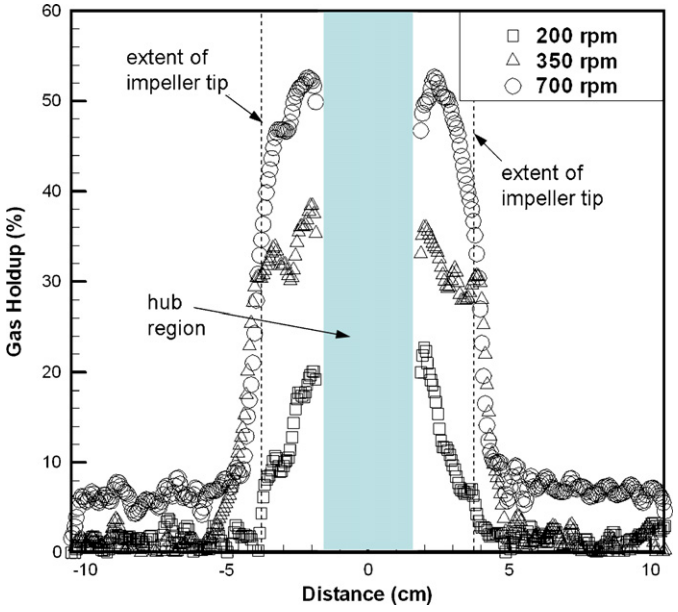

Fig. 9. Local gas holdup values along the x-axis at height $z = 0.8$ cm for $Q_g = 9$ LPM.

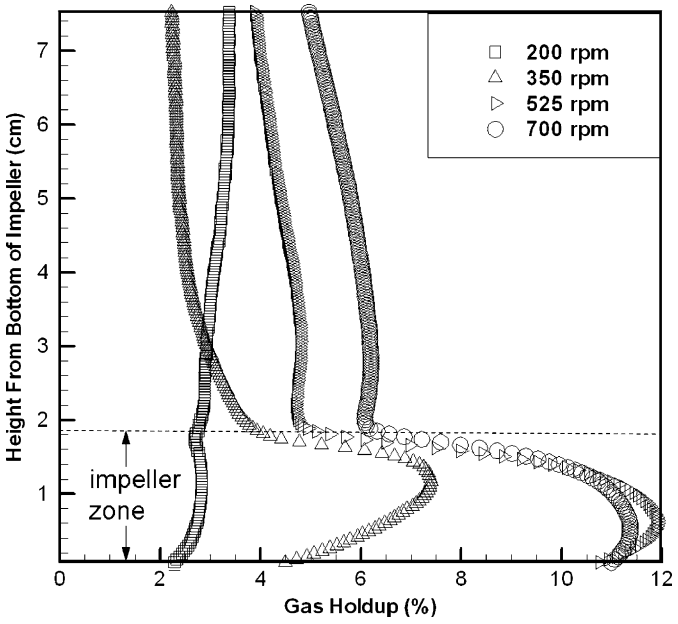

Fig. 10. Average z-slice holdup for $Q_g = 9$ LPM.

impeller is not able to disperse the gas effectively, resulting in low gas holdups outside the impeller region. Similar trends have been observed by Wang et al. (2006), although their data were obtained with a fiber-optic probe outside the impeller region. The asymmetric profiles along the x-axis (and elsewhere) are due to the slightly nonuniform gas inlet conditions.

3.4.2. Average z-slice holdup

The local time-averaged gas holdup in each z-slice can be averaged to obtain an average slice holdup (i.e., the average gas holdup as a function of vertical position). Fig. 10 shows the average slice holdup for the four different impeller speeds chosen for $Q_g = 9$ LPM. The flooded condition ($N = 200$ rpm) has a completely different trend than the other three conditions. Instead of gas holdup decreasing with increasing height, the gas holdup increases with height. Because the impeller has very little effect dispersing the gas, the decrease in pressure head with height has a big effect on the flooded regime. The decrease in pressure causes the bubbles to increase in size thereby increasing gas holdup. Also, as the bubble clusters expand and spread out, there is an increase in drag causing the bubble rise velocity to decrease which leads to higher gas holdup. For the other three conditions, the gas holdup decreases with height and has a parabolic shape in the impeller zone. The parabolic shape in the impeller zone is due to the impeller capturing the gas (Van't Riet and Smith, 1975). Another trend can be seen from the graph when excluding the flooded condition; the gas holdup increases with increasing impeller speed at all heights above the impeller zone.

Table 1
Overall average gas holdup of imaging region (CT) and tank (global)

Q (LPM)	N (rpm)	$\varepsilon_{g,t}$ (%)		
		CT	Global	Yawalkar et al. (2002)
6	350	3.4	2.9	5.7
6	700	4.8	5.0	9.0
9	200	3.0	2.9	4.7
9	350	3.5	3.3	6.7
9	525	5.9	4.5	8.7
9	700	6.9	6.0	10.4
12	325	5.4	4.8	7.6
12	700	7.0	6.4	12.3

3.4.3. Global holdup

By averaging the slice-average gas holdup values, an overall gas holdup for the imaging region is obtained. Overall gas holdup obtained using CT values and the visual technique (Saravanan and Joshi, 1996; Yawalkar et al., 2002) is presented in Table 1. As the impeller speed increases while holding Q_g constant, gas holdup increases, which has also been recorded by many authors (Thatte et al., 2004; Yawalkar et al., 2002). The CT gas holdup is highest for the condition $Q_g = 12$ LPM and $N = 700$ rpm. The CT and global gas holdup values differ slightly because the CT holdup only takes into account the imaging region, which on average, has more gas than the rest of the tank, whereas the global gas holdup values comprise the entire tank, including the area below the impeller.

The global gas holdup values from this study were compared to the correlation proposed by Yawalkar et al. (2002):

$$\varepsilon_{g,t} = 0.122\left(\frac{N}{N_{cd}}\right)^{0.64}(\text{vvm})^{0.69}(T)^{0.22}\left(\frac{D}{T}\right)^{0.14}, \quad (5)$$

where vvm is the volumetric flow rate per unit liquid volume. Eq. (5) was developed from a total of 220 data points that included both Rushton-type and pitched-blade impellers over a range of STR diameters ($T = 0.57$–2.7 m). As shown in Table 1,

the Yawalkar et al. correlation over predicts the global gas holdup; this is attributed to the small size of the custom-built STR used in this study. Yawalkar et al. claim that correlating gas holdup with respect to N/N_{cd} accounts for flow regime changes over various STR scales. However, STR diameters less than ~ 0.3 m may produce different flow conditions that may not represent those found in commercial-scale equipment,[1] which is representative of the Yawalkar correlation. Although the flow conditions of this study may not represent those found in commercial-scale equipment, the data are still very useful and can be used in CFD validation studies.

3.4.4. Error quantification

Three CT scans were taken at $Q_g = 9$ LPM and $N = 700$ rpm to determine the repeatability of the results. For the three scans, CT overall gas holdup values had a percent standard error of 6.5%.

Based on an uncertainty analysis (Figliola and Beasley, 2000), the maximum gas holdup uncertainty is $\pm 15\%$ of the reported measurements. This occurs in regions of low gas content or at low gas flow rates. Under most operating conditions, however, the gas holdup uncertainty is much lower (i.e., on the order of $\pm 5\%$ of the reported measurement when $\varepsilon_g \gtrsim 5\%$).

4. Conclusions

In this research, local time-averaged gas holdup measurements in a stirred-tank reactor were obtained using X-ray computed tomography for various operating conditions. Power consumption for different operating conditions was determined to identify various STR flow regimes. The CT slices revealed dramatic differences in gas dispersion depending on operating regime. There was very little visual difference for scans taken in the same flow regime even though there were differences in impeller speed and gas flow rates. The high resolution of the X-ray system allowed fine details such as recirculation cells behind the baffles to be visualized. Local time-averaged gas holdup was sensitive to tank design, which was shown by asymmetric recirculation cells and regions of higher gas holdup on one side of the x- and y-slices; these were attributed to an asymmetric ring sparger.

Gas holdup measurements were also quantitatively analyzed showing the differences between operating regimes. Flooded conditions showed a relatively high gas holdup near the impeller shaft while completely dispersed conditions had a uniform gas holdup outside the impeller region. Average gas holdup values for the z-slices were obtained showing how the holdup changed with height. The efficient capture of gas by the impeller leads to increased holdup in the impeller region. For the flooded condition, average gas holdup increased with height while the opposite occurred for the loaded and completely dispersed conditions. From the average z-slice holdup values, an overall average holdup value for the imaging region was determined, showing that the holdup increased as the impeller speed increased while holding Q_g constant.

[1] Reviewer provided comment.

Notation

C	impeller clearance from bottom of tank, m
D	impeller diameter, m
Fl_g	gas flow number ($Q_g N^{-1} D^{-3}$), dimensionless
H	liquid height in vessel, m
N	impeller speed, rpm
N_{cd}	impeller speed at complete dispersion, rpm
N_f	impeller speed at flooding, rpm
N_{pg}	gassed power number ($P_o \rho_L^{-1} N^{-3} D^{-5}$), dimensionless
N_r	impeller speed at recirculation, rpm
P_g	gassed power, W
Q_g	volumetric gas flow rate, $L\,\mathrm{min}^{-1}$
T	tank diameter, m
vvm	volumetric flow rate per unit liquid volume, min^{-1}

Abbreviations

CFD	computational fluid dynamics
CT	computed tomography
ECT	electrical capacitance tomography
ERT	electrical resistance tomography
STR	stirred-tank reactor

Greek letters

ε_g	local gas holdup, dimensionless
$\varepsilon_{g,t}$	total gas holdup, dimensionless
μ	linear attenuation coefficient, cm^{-1}
ρ_L	fluid density, $\mathrm{kg\,m}^{-3}$

Acknowledgments

Portions of this work were supported by the Cooperative State Research, Education, and Extension Service, US Department of Agriculture, under agreement 2004-34188-15067. Any opinions, findings, conclusions or recommendations expressed herein are those of the authors and do not necessarily reflect the views of the USDA. The X-ray facility was funded by the National Science Foundation under award number CTS-0216367 and Iowa State University.

References

Bombac, A., Zun, I., Filipic, B., Zumer, M., 1997. Gas-filled cavity structures and local void fraction distribution in aerated stirred vessel. A.I.Ch.E. Journal 43 (11), 2921–2931.

Boyer, C., Duquenne, A.M., Wild, G., 2002. Measuring techniques in gas–liquid and gas–liquid–solid reactors. Chemical Engineering Science 57, 3185–3215.

Chaouki, J., Larachi, F., Dudukovic, M.P., 1997. Noninvasive tomography and velocimetric monitoring of multiphase flows. Industrial & Engineering Chemistry Research 36, 4476–4503.

Favre, E., Voumard, P., von Stockar, U., Peringer, P., 1993. A capacitance probe to characterize gas bubbles in stirred tank reactors. Chemical Engineering Journal 52, 1–7.

Figliola, R.S., Beasley, D.E., 2000. Theory and Design for Mechanical Measurements, third ed. Wiley, New York.

Fischer, J., Bruring, S., Lubbert, A., 1992. Gas-phase properties in stirred tank bioreactors. Chemical Engineering & Technology 15 (6), 390–394.

Ford, J.J., 2006. Using X-ray computed tomography to measure local gas holdup in an aerated stirred tank reactor. M.S. Thesis, Iowa State University, Ames, IA.

Greaves, M., Barigou, M., 1988. Estimation of gas holdup and impeller power in a stirred vessel reactor. In: Fluid Mixing III, Institute of Chemical Engineers Symposium Series, vol. 108, pp. 235–255.

Halow, J.S., 1996. Electrical capacitance imaging of fluidized beds. In: Chaouki, J., Larachi, F., Dudukovic, M.P. (Eds.), Non-invasive Monitoring of Multiphase Flows. Elsevier, New York, pp. 263–307.

Hammer, E.A., Johansen, G.A., Dyakowski, T., Roberts, E.P.L., Cullivan, J.C., Williams, R.A., Hassan, Y.A., Claiborn, C.S., 2006. Advanced experimental techniques. In: Crowe, C.T. (Ed.), Multiphase Flow Handbook. Taylor & Francis, New York. pp. 14.1–14.125.

Heindel, T.J., Hubers, J.L., Jensen, T.C., Gray, J.N., Striegel, A.C., 2005. Using X-rays for multiphase flow visualization. In: Proceedings of the 2005 ASME Fluids Engineering Division Summer Meeting and Exhibition, Houston, TX, June 19–23, 2005, Paper FEDS2005-77359.

Heindel, T.J., Jensen, T.C., Gray, J.N., 2007. Visualizing fluid flows with X-rays. In: Proceedings of FEDSM2007: 5th Joint ASME/JSME Fluids Engineering Conference, San Diego, CA, July 30–August 2, 2007, Paper FEDSM2007-37023.

Heindel, T.J., Gray, J.N., Jensen, T.C., 2008. An X-ray system for visualizing fluid flows. Flow Measurement and Instrumentation, to appear.

Holden, P.J., Wang, M., Mann, R., Dickin, F.J., Edwards, R.B., 1998. Imaging stirred-vessel macromixing using electrical resistance tomography. A.I.Ch.E. Journal 44 (4), 780–790.

Hubers, J.L., Striegel, A.C., Heindel, T.J., Gray, J.N., Jensen, T.C., 2005. X-ray computed tomography in large bubble columns. Chemical Engineering Science 60 (22), 6124–6133.

Kapic, A., Heindel, T.J., 2006. Correlating gas–liquid mass transfer in a stirred-tank reactor. Transactions of IChemE, Part A, Chemical Engineering Research and Design 84 (A3), 239–245.

Ketcham, R.A., Carlson, W.D., 2001. Acquisition, optimization and interpretation of X-ray computed tomography imagery: applications to the geosciences. Computers and Geosciences 27, 381–400.

Khopkar, A.R., Rammohan, A.R., Ranade, V.V., Dudukovic, M.P., 2005. Gas–liquid flow generated by a rushton turbine in stirred vessel: CARPT/CT measurements and CFD simulations. Chemical Engineering Science 60 (8–9), 2215–2229.

Kumar, S.B., Dudukovic, M.P., Toseland, B.A., 1997. Measurement techniques for local and global fluid dynamic quantities in two and three phase systems. In: Chaouki, J., Larachi, F., Dudukovic, M.P. (Eds.), Non-invasive Monitoring of Multiphase Flows. Elsevier, New York, pp. 1–45.

Lu, W.M., Ju, S.J., 1987. Local gas holdup, mean liquid velocity, and turbulence in an aerated stirred tank using hot-film anemometry. Chemical Engineering Journal 35 (1), 9–17.

Nagase, Y., Yasui, H., 1983. Fluid motion and mixing in a gas–liquid contactor with turbine agitators. Chemical Engineering Journal 27 (1), 37–47.

Nienow, A.W., 1998. Hydrodynamics of stirred bioreactors. Applied Mechanics Reviews 51 (1), 3–32.

Nienow, A.W., Wisdom, D.J., Middleton, J.C., 1977. The effect of scale and geometry on flooding, recirculation, and power in gassed stirred vessels. In: Proceedings of the 2nd European Conference on Mixing, Cambridge, England, pp. 1–16.

Nienow, A.W., Warmoeskerken, M.M.C.G., Smith, J.M., Konno, M., 1985. On the flooding/loading transition and the complete dispersal condition in aerated vessels agitated by a Rushton-turbine. In: Proceedings of the 5th European Conference on Mixing, Wurtsburg, West Germany, pp. 143–154.

Ranade, V.V., Deshpande, V.R., 1999. Gas–liquid flow in stirred reactors: trailing vortices and gas accumulation behind impeller blades. Chemical Engineering Science 54 (13–14), 2305.

Rushton, J.H., Bimbinet, J.J., 1968. Holdup and flooding in air liquid mixing. The Canadian Journal of Chemical Engineering 46, 16–21.

Saravanan, K., Joshi, J.B., 1996. Fractional gas hold-up in gas inducing type of mechanically agitated contactors. The Canadian Journal of Chemical Engineering 74 (1), 16–30.

Smith, J.M., Warmoeskerken, M.M.C.G., 1985. The dispersion of gases in liquids with turbines. In: Proceedings of the 5th European Conference on Mixing, Wurtsburg, West Germany, pp. 115–126.

Supardan, M.D., Masuda, Y., Maezawa, A., Uchida, S., 2004. Local gas holdup and mass transfer in a bubble column using an ultrasonic technique and a neural network. Journal of Chemical Engineering of Japan 37 (8), 927–932.

Takenaka, K., Takahashi, K., 1996. Local gas holdup and gas recirculation rate in an aerated vessel equipped with a Rushton turbine impeller. Journal of Chemical Engineering of Japan 29 (5), 799–804.

Thatte, A.R., Ghadge, R.S., Patwardhan, A.W., Joshi, J.B., Singh, G., 2004. Local gas holdup measurement in sparged and aerated tanks by γ-ray attenuation technique. Industrial & Engineering Chemistry Research 43 (17), 5389–5399.

Utomo, M.B., Sakai, T., Uchida, S., Maezawa, A., 2001. Simultaneous measurement of mean bubble diameter and local gas holdup using ultrasonic method with neural network. Chemical Engineering & Technology 24 (5), 493–500.

Van't Riet, K., 1975. Turbine agitator hydrodynamics and dispersion performance. Ph.D. Thesis, Delft University of Technology, Delft, The Netherlands.

Van't Riet, K., Smith, J.M., 1975. Trailing vortex system produced by Rushton turbine agitators. Chemical Engineering Science 30 (9), 1093–1105.

Veera, U.P., Patwardhan, A.W., Joshi, J.B., 2001. Measurement of gas hold-up profiles in stirred tank reactors by gamma ray attenuation technique. Transactions of IChemE, Part A, Chemical Engineering Research and Design 79 (6), 684–688.

Wang, M., Dorward, A., Vlaev, D., Mann, R., 2000. Measurements of gas–liquid mixing in a stirred vessel using electrical resistance tomography (ERT). Chemical Engineering Journal 77 (1), 93–98.

Wang, W.J., Mao, Z.S., Yang, C., 2006. Experimental and numerical investigation on gas holdup and flooding in an aerated stirred tank with Rushton impeller. Industrial & Engineering Chemistry Research 45 (3), 1141–1151.

Warmoeskerken, M.M.C.G., Smith, J.M., 1982. Description of the power curves of turbine stirred gas–liquid dispersions. In: Proceedings of the Fourth European Conference on Mixing, Noordwijkerhout, Netherlands, pp. 237–246.

Warmoeskerken, M.M.C.G., Smith, J.M., 1985. Flooding of disc turbines in gas–liquid dispersions: a new description of the phenomenon. Chemical Engineering Science 40 (11), 2063–2071.

Warmoeskerken, M.M.C.G., Feijen, J., Smith, J.M., 1981. Hydrodynamics and power consumption in stirred gas–liquid dispersion. In: Fluid Mixing, vol. 64, Institute of Chemical Engineers Symposium, pp. J1–J14.

Warsito, W., Fan, L.-S., 2001. Measurement of real-time flow structures in gas–liquid and gas–liquid–solid flow systems using electrical capacitance tomography (ECT). Chemical Engineering Science 56, 6455–6462.

Warsito, W., Fan, L.-S., 2005. Dynamics of spiral bubble plume motion in the entrance region of bubble columns and three phase fluidized beds using 3D ECT. Chemical Engineering Science 60, 6073–6084.

Warsito, W., Ohkawa, M., Kawata, N., Uchida, S., 1999. Cross-sectional distributions of gas and solid holdups in slurry bubble column investigated by ultrasonic computed tomography. Chemical Engineering Science 54, 4711–4728.

Yawalkar, A.A., Pangarkar, V.G., Beenackers, A.A.C.M., 2002. Gas holdup in stirred tank reactors. The Canadian Journal of Chemical Engineering 80, 158–166.

Zhang, J., Chou, C., Jensen, T.C., Gray, J.N., 2005. Development of a high-resolution CT system and 3D data visualization tools. In: Thompson, D.O., Chimenti, D.E. (Eds.), Review of Progress in Quantitative Nondestructive Evaluation, vol. 24. American Institute of Physics, pp. 686–693.